Journal of Wind Engineering & Industrial Aerodynamics 210 (2021) 104524

Contents lists available at ScienceDirect

Journal of Wind Engineering & Industrial Aerodynamics

journal homepage: www.elsevier.com/locate/jweia

The impact of urban block typology on pollutant dispersion

Fabiana Trindade da Silva *, Neyval Costa Reis Jr., Jane Meri Santos, Elisa Valentim Goulart, Cristina Engel de Alvarez

Department of Environmental Engineering, Universidade Federal do Espírito Santo, Brazil, Av. Fernando Ferrari 514, 29.075-910, Vitoria, ES, Brazil

ARTICLE INFO

Keywords:
Urban morphology
Block typology
Pollutant dispersion
Urban indices
Urban planning

ABSTRACT

Block typology is a central component for urban planning and a key element to represent the urban form, which affects the airflow. Therefore, the aim of this work consists of investigating the impact of different urban block typologies in urban pollutant dispersion. Five typologies derived from real cities were investigated using the computational fluid dynamics technique: single-block, detached buildings, central courtyard, inner courtyards, and row. The numerical simulations were performed using URANS (Unsteady Reynolds-Averaged Navier-Stokes) equations and the $\kappa - \omega$ SST model to represent the turbulence effects. The model was validated using wind tunnel experimental data. Urban air quality was assessed using five parameters: mean age of air, net escape velocity, pollutant concentration at pedestrian level, and pollutant mass fluxes towards the urban canopy and outwards from it. The results showed that the single-block typology revealed an average pollutant concentration at pedestrian height 80% lower than that estimated in the detached building typology, which presented the highest concentration, probably due to the highest aspect ratio associated with permeable facades. Further, the higher the wind velocity, the lower the mean age of air. Finally, the unbuilt areas' disposition within the block proved to be the more important parameter influencing the pollutant dispersion.

1. Introduction

Urban air pollution is associated with a wide range of acute and chronic health effects (Brunekreef and Holgate, 2002; World Health Organization, 2016). The World Health Organization (World Health Organization, 2016) pointed out that about 3 million deaths occurred in 2016 associated with outdoor air pollution. Urban planning is considered an important tool to improve air quality conditions. It is noteworthy that the urban dynamic takes place essentially at the pedestrian level (Gehl and Svarre, 2013), and therefore it is especially important to assess the pedestrian wind environment for urban planning (An et al., 2019a; Ayo et al., 2015; Kurppa et al., 2018; Ramponi et al., 2015; Yuan et al., 2014a). Urban morphology influences the wind flow which is affected by multiple combinations of buildings' arrangement and density, as well as on individual buildings' shape and dimensions (Ramponi et al., 2015). Indeed, many studies have pointed out that the urban morphology is a key factor to understand air flow and pollutant dispersion within the urban canopy (Buccolieri et al., 2015; Carpentieri and Robins, 2015a; Kurppa et al., 2018; Peng et al., 2019a; Ramponi et al., 2015; Yuan et al., 2019b).

The computational fluid dynamics (CFD) technique has been successfully used in a wide number of studies to investigate air pollutant dispersion in urban areas. These researchers have investigated the impact of urban morphology characteristics such as density and permeability (An et al., 2019b; Ng and Chau, 2014; Peng et al., 2019a; Yang et al., 2020), block shape (Moonen et al., 2012; Yuan et al, 2014b, 2019a), and building height (Carpentieri and Robins, 2015b; Chen et al., 2017b; Hang et al., 2015; Lin et al., 2014a) on the pollutant dispersion in urban-like areas. Also, some studies have analyzed the impact of urban morphology on cities' breathability using the mean age of air and fluxes towards the canopy (Buccolieri et al., 2015; Chen et al., 2017a; Hang et al., 2018; Shen et al., 2017a). Several studies (An et al., 2019b; Buccolieri et al., 2015; Carpentieri and Robins, 2015b; Hang et al, 2015, 2018; Ng and Chau, 2014; Sha et al., 2018) use the normalized mean square error (NMSE) to evaluate the accuracy of CFD simulations compared with the experimental data. As indicated by Herring and Huq (2018) and Schatzmann et al. (2010) the value for NMSE should be less than 4. As with the mentioned studies, our study found a value of less than 1.5. Therefore, the CFD method can be considered an accurate tool for quantifying the urban wind environment and pollutant dispersion.

* Corresponding author.
E-mail addresses: fabianatrindade.silva@gmail.com (F. Trindade da Silva), neyval@pq.cnpq.br (N.C. Reis), jane.santos@pq.cnpq.br (J.M. Santos), elisa.goulart@ufes.br (E.V. Goulart), cristina.engel@ufes.br (C. Engel de Alvarez).

https://doi.org/10.1016/j.jweia.2021.104524
Received 8 July 2020; Received in revised form 18 December 2020; Accepted 5 January 2021
Available online 25 January 2021
0167-6105/

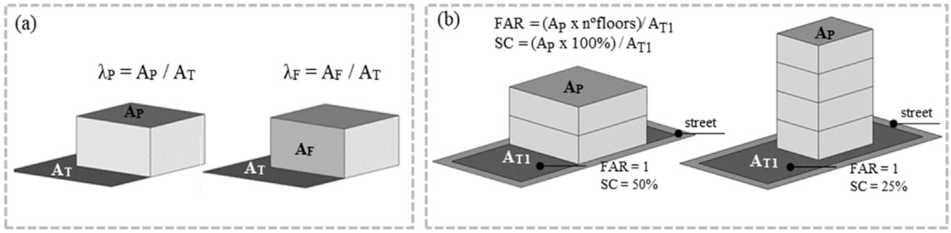

Fig. 1. (1.5 column) – Schematic illustration of urban metrics: (a) planar area density (λ_p) and frontal area density (λ_f); and (b) urban indices: floor area ratio (FAR) and surface coverage (SC).

Furthermore, an important aspect of CFD simulations is the turbulence model selection. Large Eddy Simulation (LES) and Reynolds-averaged Navier-Stokes (RANS) are turbulence modelling strategies well reported in the literature to simulate the turbulence effects on atmospheric dispersion in urban areas. The accuracy of LES and the limitations of steady RANS have been reported by Blocken (2015b, 2014), Tominaga et al. (2008a), and Xie and Castro (2009), for instance. One of the steady RANS limitations is the difficulty to reproduce the periodic releases of vortexes (vortex shedding) due to the presence of several bluff bodies, which generates periodic low-frequency movements (Iaccarino et al., 2003; Mannini et al., 2010). Given that and the high computational costs of LES, the unsteady RANS (URANS) is an alternative for solving the RANS equations affording a transient solution at a low computational cost. Usually, the integration time interval required to achieve representative averages is hundreds of times larger than the flow characteristic time scale (Tominaga and Stathopoulos, 2017). Furthermore, studies such as Iaccarino et al. (2003), Mannini et al. (2010), and Tominaga and Stathopoulos (2018) have reported good results of the URANS method if compared to the steady RANS showing an improvement in the accuracy of the mean concentration estimation.

Although CFD simulations easily allow parametric studies to evaluate different design configurations, there are still only a few studies about the

Fig. 2. (2 column) – Satellite view and figure-ground of selected cities sample: (a) Tokyo; (b) Hong Kong; (c) Shanghai; (d) Barcelona; (e) Paris; (f) London; (g) New York; (h) Sao Paulo. Source: Adapted from Google Earth (2019).

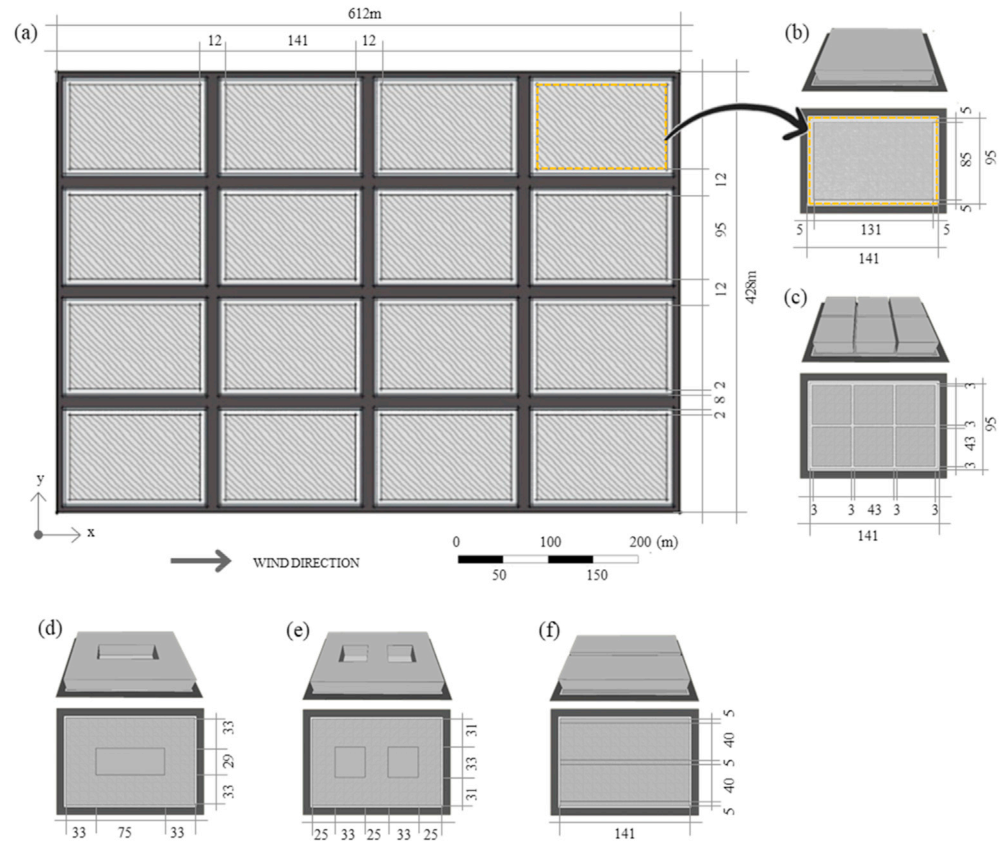

Fig. 3. (2 column) – Schematic representation of (a) the urban block fabric and urban block typologies: (b) single-block; (c) detached buildings; (d) courtyard; (e) inner courtyards; (f) rows.

impact of block typology on air quality (Carpentieri and Robins, 2015a; Guo et al., 2017; Peng et al., 2019a; You et al., 2017) which is a central component of urban planning. These studies have highlighted the importance of properly representing urban geometry. Nonetheless, most of the urban quality studies uses an idealized array (Chen et al., 2017a; Hang et al., 2015; Lin et al., 2014b), usually represented by square blocks equally spaced. However, as pointed out by (Yuan and Ng, 2014), block typology simplification can generate an idealized or unrealistic city version. In contrast, real urban areas are highly heterogeneous, with a wide range of density and typologies within the same city. For these reasons, a block typology method can represent an intermediary approach between studying real cities, which produces results to a specific situation, and studying an idealized array that does not represent a real urban area. Therefore, a representation of an urban block in numerical simulations can be simple enough to be generic, yet complex enough to represent reality. Also, to support the urban planning process, the urban block parameterization used in the studies must be based on real cities' environments.

In this context, some studies investigate simplified scenarios derived from the predominant typology of a specific region (Carpentieri and Robins, 2015a; Yuan et al., 2019b) so they resemble real city environments. Other studies analyze the role of a specific block typology in pollutant dispersion. For instance, the single-block typology was investigated in Buccolieri et al. (2015) and Yang et al. (2019a), detached buildings in Peng et al. (2019b) and Bady et al. (2008), courtyards in Kurppa et al. (2018) and Gronemeier and Sühring (2019); and rows in Yuan et al. (2019a, 2014a). These works investigated the influence of block typology characteristics, such as length, width, building height, and porosity, and its variations for the same typology. However, there has not been found by the authors of the present work at this point, a study concerning the influence of different urban block typologies on air quality.

Moreover, some parameters used to assess outdoor ventilation performance have also been applied to evaluate urban air quality, for instance, mean age of air (τ_p), purging flow rate (PFR), and net escape velocity (NEV) (Peng et al., 2019b). These variables have shown a good correlation with urban morphological parameters (Peng et al., 2019a). Additionally, convective and turbulent pollutant mass fluxes outwards of the urban canopy have been analyzed as pollutant removal contributors to evaluate city breathability (Shen et al., 2017b). The city breathability reflects the outdoor ventilation performance to remove and dilute pollutants as well as heat and moisture (Buccolieri et al., 2015).

Parameters like the planar area density (λ_p) and the frontal area density (λ_f) are commonly used metrics to describe urban density in urban air quality studies (Hang et al., 2015; Ramponi et al., 2015; Shirzadi et al., 2018). However, these metrics are still far from the usual urban planning indices. Some of the most common urban indices used for urban planning around the world are FAR (floor area ratio), SC (surface coverage), and H (building height). These indices are well consolidated in urban planning and adopted in countries like Spain, France, Japan, United States, Brazil, and others. More recently, these urban planning indices have been used in air quality studies (Cheshmehzangi and Butters, 2016; Peng et al., 2019a; Yang et al., 2019b), but still in very few studies. Fig. 1 illustrates the urban metrics λ_p and λ_f and urban indices FAR and SC. The metrics λ_p and SC represent the same parameter, the building coverage ratio. On the other hand, λ_f correlates the built area with building height, while FAR represents the built volume. However, while the values of λ_p and λ_f consider the ratio between the built area and the total area (including the street area), the values of FAR and SC consider the only ratio between the built area and block area (excluding the street area).

The main objective of this work is to investigate the impact of different urban block typologies in urban pollutant dispersion to support urban planning decisions. Five typologies derived from real cities and

Table 1
(Single) Metric values for the urban blocks.

CASE	BLOCK TYPOLOGY	λp	λf	FAR	SC (%)	H (m)
01	Single-block	0.63	0.18	5	83	18
02	Detached buildings	0.63	0.17	5	83	18
03	Courtyard	0.64	0.19	5	84	18
04	Inner courtyards	0.64	0.19	5	84	18
05	Row	0.63	0.19	5	83	18

Legend: P1 – parallel to the wind; P2 – perpendicular to the wind; W - width.

literature review were investigated using the computational fluid dynamics technique: single-block, detached buildings, central courtyard, inner courtyards, and row. Additionally, the geometric dimensions were based on the usual indices values for FAR, SC, and H from real cities. Finally, the urban quality was analyzed based on τ_p, NEV, pollutant concentration at pedestrian level, and convective and turbulent pollutant mass fluxes towards and outward the urban canopy.

2. Method

2.1. Description of urban blocks typologies

Five urban block typologies were analyzed: single-block, detached buildings, central courtyard, inner courtyards, and row. The chosen five block typologies represent common typologies found in the literature and real cities. Fig. 2 shows aerial views of central regions in real large cities chosen as a reference in different continents: Hong Kong, Tokyo, and Shanghai (Asia); Barcelona, Paris, and London (Europe); and New York and Sao Paulo (North and South America). Samples of these regions highlighted in Fig. 2 comprise a 500 m radius taken from the densest region in each city. It is important to emphasize that these samples represent typical central regions and not the entire city typology. An analysis of the most common typologies indicates that single-block occurs in Asian (Fig. 2a), American cities (Fig. 2h), and London (Fig. 2f); detached buildings is a more common typology in Asian (Fig. 2b), and American cities (Fig. 2h); courtyard typology is very expressive in European cities (Fig. 2d and e); and, finally, row typology is found in Asian and American cities (Fig. 2c).

European cities present more uniform urban indices values in comparison with Asian and American cities. For this reason, the metrics values used in this study (λ_p, λ_f, *H/W*, *H*, *FAR*, and *SC*) for the urban blocks were based on European cities and consider urban blocks of approximately 95 × 140 m and a 12 m street width (*W*). Also, to understand the impact of urban block typologies on the urban pollutant dispersion it is important to maintain similarity between geometries to be able to evaluate the isolated influence of block typology. Therefore, the five chosen scenarios present the same urban layout, i.e. urban blocks and streets (Fig. 3a), and values of *FAR*, *SC*, and *H* (*FAR* equal 5, *SC* about 80%, and 18 m as building height, corresponding to mean values of European cities as shown in Table 1).

Fig. 3b-f displays the five urban block typologies investigated in the present work. Although the same urban indices values were imposed for the five urban block typologies, the geometric design of each block has particular features. The spaces between buildings in the blocks lead to different frontal area ratio (λ_f) and canyons aspect ratio (*H/W*) (see Table 1). The impact of these differences on pollutant dispersion is investigated in the results section.

2.2. Mathematical modelling and numerical simulation setup

The computational domain comprises sixteen urban blocks; four in the *y*-axis and four in the *x*-axis. Therefore, the computational domain size is 612 m (34 *H*, length) × 428 m (23.8 *H*, width) × 216 m (12 *H*, height), where $H = 18$m. The domain height was set as 12 *H* as suggested by Castro et al. (2017). Yuan et al. (2019a, 2014b) suggested that the turbulence model SST $\kappa-\omega$ proposed by Menter (1994) is a good turbulence modelling strategy for wind flow and air pollutant dispersion simulations in urban areas due to the low computational cost and adequate results accuracy. This is a model that combines the $\kappa-\omega$ and $\kappa-\varepsilon$ models, such that $\kappa-\omega$ is used in the internal region of the boundary layer eliminating the need for a wall function while $\kappa-\varepsilon$ is used in the free shear flow region. Therefore, in the present study, the URANS approach was employed with the SST $\kappa-\omega$ turbulence model. The FLUENT 19.2 software, which employs the finite volume method, was used to solve the mass, momentum, and mass of chemical species conservation equations including the equations associated with the SST $\kappa-\omega$ model.

The boundary conditions for all domain boundaries are presented in Table 1. The periodic boundary conditions were imposed on the domain boundaries, helping to reduce the complexity of the problem by allowing the representation of a single segment of the simulated city section. This strategy helps to reduce the mesh and size of the computational domain, as carried out by Fuka et al. (2018), Kristóf and Füle (2017) and, Shen et al. (2015). The flow is maintained by a pressure gradient in the *x*-direction, given by

$$\frac{d\overline{p}}{dx} = -\rho\frac{u_*^2}{H_T} \tag{1}$$

where u_* is the friction velocity equal to 0.134 m/s, H_T is the total domain height and ρ is the air absolute density. Therefore, the pressure gradient ($d\overline{p}/dx$) is equal to 10.18×10^{-5} Pa/m. The source of pollutant is configured as an area distributed along the streets, to simulate the emission of pollutants generated by the traffic. The pollutant was released continuously with a constant and uniform emission rate equal to 5×10^{-3} kg/m^{2}s, considered chemically inert, and having the same density as air.

The grid resolution complies with the guidelines proposed by the Working Group of the Architectural Institute of Japan (AIJ) (Tominaga et al., 2008b) for computational fluid dynamics (CFD) simulations of pedestrian wind environment around buildings. The computational domain was discretized using a structured hexahedral grid; the number of elements for each case varies according to the geometry (from about 4.000.000 to about 6.200.000 elements). The grid resolution should be fine enough to capture the important physical phenomena with sufficient resolution. COST guidelines (Franke et al., 2007) indicate that in the area of interest, at least 10 cells per cube root of the building volume should be used. Accordingly, the number of cells per obstacle should be at least $\Delta = \frac{h}{16}$ (Castro et al., 2017). Therefore, given the need for a refined mesh near the pedestrian height, a cell of 1 m was set close to solid surfaces ($\Delta = h/18$) with a growth rate of 1.2 outwards from these surfaces. To refine the mesh to adequately capture the physical phenomena between the ground and the pedestrian level, the inflation layer technique (with 5 layers) was applied close to the ground and buildings' surfaces with the first layer height defined as 0.06 m. The first layer size was defined to achieve a z_w^+(Equation (2)) smaller than 1, indicated for the SST $\kappa-\omega$ turbulence model (ANSYS Academic Research, 2018).

$$z_w^+ = \frac{u_* z_w}{\nu_{air}} \tag{2}$$

where z_w is the distance from a wall (m) and ν_{air} kinematic viscosity of air (m^{2}s^{-1}).

The European Cooperation in the field of Scientific and Technical Research (COST) indicates that three different meshes should be tested (Franke et al., 2007) to guarantee mesh independence and that the number of grid cells should be at least 1.5 times larger in each dimension for mesh refinement (Ferziger and Perić, 2002). The base grid was found refined enough to guarantee mesh independence. The grid sensitivity analysis is presented in Section 3.2.

The time step was set taking into account the Strouhal number (*St*)

Table 2
(2 column) Summary of settings for the CFD simulation.

	Settings for CFD simulations
Computational domain size	612 m × 428 m × 216 m
Grid type	Structured hexahedral grid
Grid resolution	From 4.000.000 to about 6.200.000 elements. Approximated number of elements per typology: Single-block: 4.000.0000; Detached buildings: 6.200.000; Central courtyard: 5.800.000; Inner courtyards: 5.900.000; Row: 5.700.000
Boundary conditions	Periodic conditions on the two lateral borders, inlet, and outlet Stationary wall no-slip condition on the ground and buildings walls Stationary wall free-slip condition on the top
Turbulence model	SST $\kappa - \omega$ model
Solving algorithms	SIMPLE algorithm for pressure-velocity coupling Gradient: Least Squares Cell-Based Pressure: Second Order Momentum: Second-Order Upwind Turbulent Kinect Energy: Second-Order Upwind Specific Dissipation Rate: Second-Order Upwind Transient Formulation: Second-Order Implicit
Convergence criteria	1×10^6 for all variables

defined by Equation (3).

$$S_t = \frac{fH}{U_H} \tag{3}$$

where *St* is defined according to the Reynolds number (*Re*) (for *Re* equal to 10^5, *St* is set as 0.2), and *f* is the frequency of vortex shedding and U_H is the wind speed at the building height. As a result, the time step was $\Delta_T = 0.5s$ and the simulations run for about 200 H/U_H. To prevent the pollutant mass from re-entering the domain due to the periodic boundary conditions, a sponge layer was applied to the pollutant concentration field at the outlet. The summarized settings for the simulations are described in Table 2.

Model validation was performed using the experimental data provided by Castro et al. (2017) and Fuka et al. (2018). All details regarding experimental details, numerical setup, sensitivity grid test, and results are presented in Section 3.

2.3. Assessment of ventilation and pollutant dispersion at pedestrian height

In this study, to assess the ventilation and pollutant dispersion at the pedestrian height, the mean concentration and the mean velocity magnitude at pedestrian height (2 m) were firstly determined. Sequentially, to understand the dispersion at the pedestrian volume, the following indices were adopted: convective flux ($\overline{F}_c$), turbulent flux ($\overline{F}_t$), total flux ($\overline{F}_{total}$), mean age of air (τ_p), purging flow rate (PFR), and net escape velocity (NEV). The convective, turbulent, and total fluxes were calculated at three sections as shown in Fig. 4, aiming to evaluate the dilution and removal of pollutants out of the canopy (vertical fluxes) and within the canopy (horizontal fluxes). $\tau_p$is commonly used to assess the breathability (Buccolieri et al., 2015; Hang et al., 2015) which reflects the ventilation potential of a region. The concept of PFR is used to predict the net rate of removing pollutants in the urban domain, it was introduced by Bady et al. (2008) and adopted in studies by Shen et al. Shen et al. (2017b) and Peng et al. (2019a). Finally, NEV is based on the concept of PFR and was proposed by Hang et al. (2012b), it represents the net capacity of removing or diluting pollutants from the pedestrian volume by mean convective and turbulent fluxes.

As previously mentioned the source is located in all street domains. The pollutant concentration at pedestrian height (2 m) is normalized as indicated in (Fuka et al., 2018) and described in Equation (4).

$$\overline{c}^* = \overline{c}_{ped} \frac{U_H H^2}{\dot{m}} \tag{4}$$

where $\overline{c}^*$is the dimensionless concentration, $\overline{c}_{ped}$is the pollutant concentration at pedestrian level [kg/m^3], and $\dot{m}$ is the source emission rate of pollutants [kg/s].

The convective and turbulent pollutant mass fluxes outward from the urban canopy (*z*-axis) or in the main flow direction (*x*-axis) can be calculated as presented in Equations (5) and (6).

$$\overline{F}_c = \overrightarrow{V}.\overrightarrow{n}\overline{c} \tag{5}$$

$$\overline{F}_t = -\frac{\mu_t}{Sc_t}\left[\frac{\partial \overline{c}}{\partial n}\right] \tag{6}$$

$$\overline{F}_{total} = \overline{F}_c + \overline{F}_t \tag{7}$$

where $\overrightarrow{V}$ is the velocity vector, $\overrightarrow{n}$ is the normal unit vector to leeward boundaries or street roofs, $\overline{c}$ is the pollutant concentration (kg/m^3). Both the velocity and concentration are spatially averaged quantities. The overbar on all variables is related to Reynolds averaging. μ_t is the turbulent viscosity, Sc_t is the turbulent Schmidt number (taken as $\mathrm{Sc_t} = 0.7$). The fluxes are normalized by the pollutant mass flux at the source $\overline{F}^* = \overline{F}/\dot{m}$.

$\tau_p$is calculated as shown in Equation (8) and represents the mean time required for the inflow air to reach a certain point in the space. Lower values of $\tau_p$indicate better ventilation and consequently better air quality in the pedestrian height. $\tau_p$is normalized as proposed by (Shen et al.,

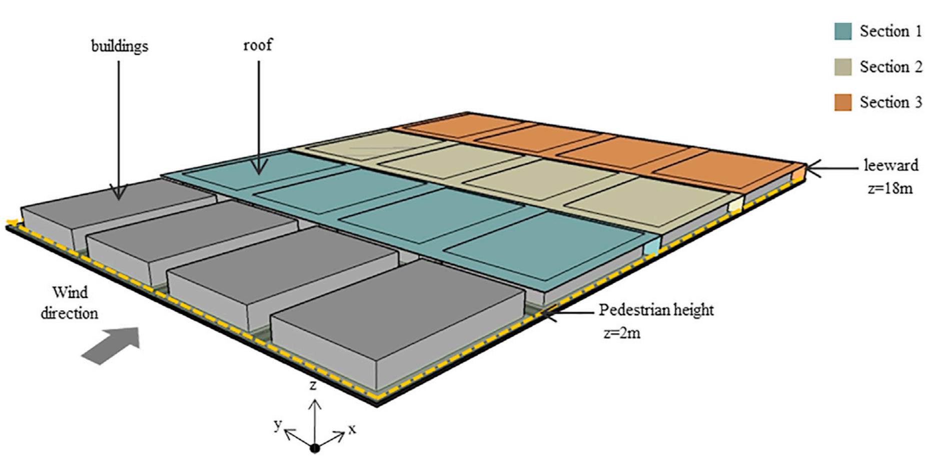

Fig. 4. (1.5 column) – Scheme of the division of the sections in the x-direction and the indication of pedestrian height.

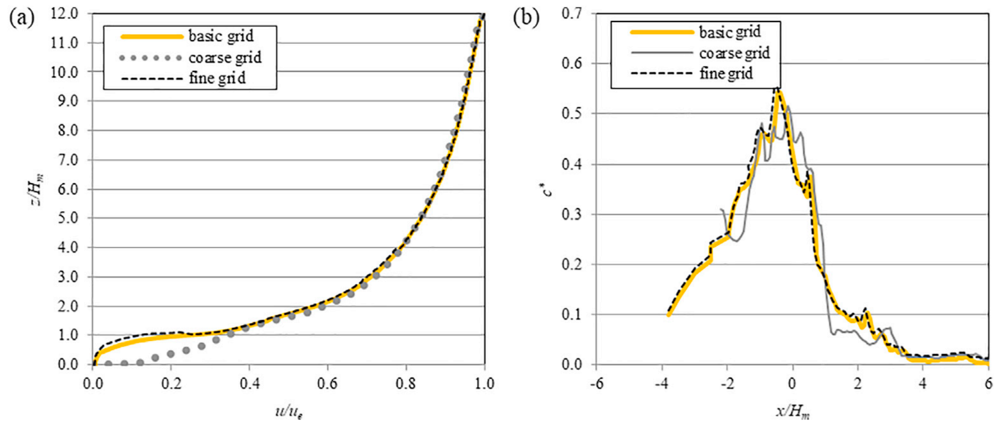

Fig. 5. (2 column) – (a) Normalized mean velocity profiles and (b) normalized mean concentration for 0° wind direction for different grids sizes.

2017a) (Equation (9)).

$$\tau_p = \frac{\bar{c}_{ped}}{\dot{m}} \tag{8}$$

$$\tau_p^* = \frac{\tau_p Q}{\forall_{ped}} \tag{9}$$

where $\bar{c}_{ped}$is the integrated concentration in $\forall_{ped}$which represents the volume (m^3) of the entire pedestrian space calculated by multiplying the area of the streets by the pedestrian height. Q is the volumetric air flow rate (m^3/s) calculated as the product of the inlet opening area (up to the pedestrian height) and the velocity far upstream at the entrance to the canopy at the pedestrian height. $\dot{m}$ is the pollutant emission rate ($\dot{m} = 5 \times 10^{-3}$ kg/s).

The concept of PFR was introduced by Bady et al. (2008) and adopted in studies by Shen et al. (2017b) and Peng et al. (2019a). PFR is used to predict the net rate of pollutant mass removal in the urban domain (Equation (10)).

$$PFR = \frac{\dot{m}\, \forall_{ped}}{\bar{c}_{ped}} \tag{10}$$

NEV represents the net ability to remove and dilute pollutants from the pedestrian volume by convective flows and turbulent diffusion, it is based on the concept of PFR and was proposed by Hang et al. (2012a) as indicated in Equation (11).

$$NEV = \frac{PFR}{A_p} \tag{11}$$

where A_p is the entire area of the boundaries for the entire pedestrian volume.

3. Validation and mesh sensitivity

3.1. Model validation

The experimental data used for the model validation are described in detail by Castro et al. (2017) (fluid flow) and Fuka et al. (2018) (pollutants mass transfer). The experiments were conducted in the wind tunnel at the EnFlo laboratory of the University of Surrey in England. The urban canopy was represented using a square arrangement of 294 rectangular blocks with 21 blocks distributed along the x-axis and 14 on the y-axis. The dimensions of the blocks were: $H \times 2H \times H$, being H the building height equal to 70 mm. The freestream velocity in the approaching flow was 2 m/s. Experimental data available for building array orientations of $\theta = 0°$ and 90°, to the wind direction were used in the present work for the numerical model validation. The pollutant was released continuously and at a steady rate from a point source at the ground.

The wind tunnel experiments used to validate the numerical simulation were conducted using a reduced scale (1:250). The computational domain used in the simulations to validate the model followed the dimension of the experiments. Therefore, the full-scale investigated scenarios (H = 18m in full-scale) were scaled down for the numerical simulations as in similar studies (An et al., 2019a; Carpentieri and Robins, 2015c; Hang et al., 2015; Ricci et al., 2017). The computational domain size attends the recommendations of Castro et al. (2017) who stated that the array should have at least 18 blocks to attain results that were essentially independent of domain size due to the type of boundary conditions used in the simulations which are the same type as those used in the present work. These authors utilize in their LES and DNS simulations a domain of $12\,H \times 12\,H \times 12H$. Therefore, for the present research, the computational domain was $12\,H \times 12\,H \times 12H$, where $H = 0.07$ m comprising a total of 24 blocks; 4 blocks on the x-axis, and 6 blocks on the y-axis. The blocks were equally distanced on both axes by H. The mesh size contained about 4,000,000 grid cells with 18 grid cells within 0.004 m from the solid surfaces. All other parameters were set as described in Castro et al. (2017) and Fuka et al. (2018).

The grid sensitivity was verified using three different mesh sizes: a coarse grid (2.600.000), a basic grid (4.000.000 elements), and a fine grid (6.000.000). Fig. 5 (a,b) exhibits the analysis of the mesh independency for the normalized mean velocity profiles and normalized mean concentration for the 0° wind direction. The coarse grid shows a higher u/u_e close to the ground compared to the basic and fine grid. Also, for the coarse grid, the scalar behavior is slightly different from the other finer grids. Otherwise, that is an acceptable correspondence between the basic and the fine grid, showing that the utilization of the basic grid is adequate.

Fig. 6 shows the numerical and experimental results for the 0° and 90° array orientations of normalized mean velocity and concentration profiles. Correspondingly to the procedure described by Castro et al. (2017), for the velocity profiles, data have been spanwise averaged at each height, using the values from 20 profiles (equally distributed throughout the domain axis) taken at different spanwise locations. The velocity is normalized as indicated in (Castro et al., 2017) and the concentration is normalized as indicated in (Fuka et al., 2018). Velocity was normalized using the velocity at the domain top (U_e) and concentration was normalized as indicated in the main manuscript and that reference velocity was taken as the flow velocity at $z = 2.8H$.

In general, the numerical results obtained using the SST $\kappa - \omega$ model (Fig. 6 – dashed line) are in good agreement with the wind tunnel data (Fig. 6 – symbols). Willemsen and Wisse (2002) reported that wind tunnel experiments could conservatively be estimated to have a standard measurement error of 20%, highlighting the uncertainties in wind tunnel data. The 20% error is also adopted in An et al. (2019) to evaluate the

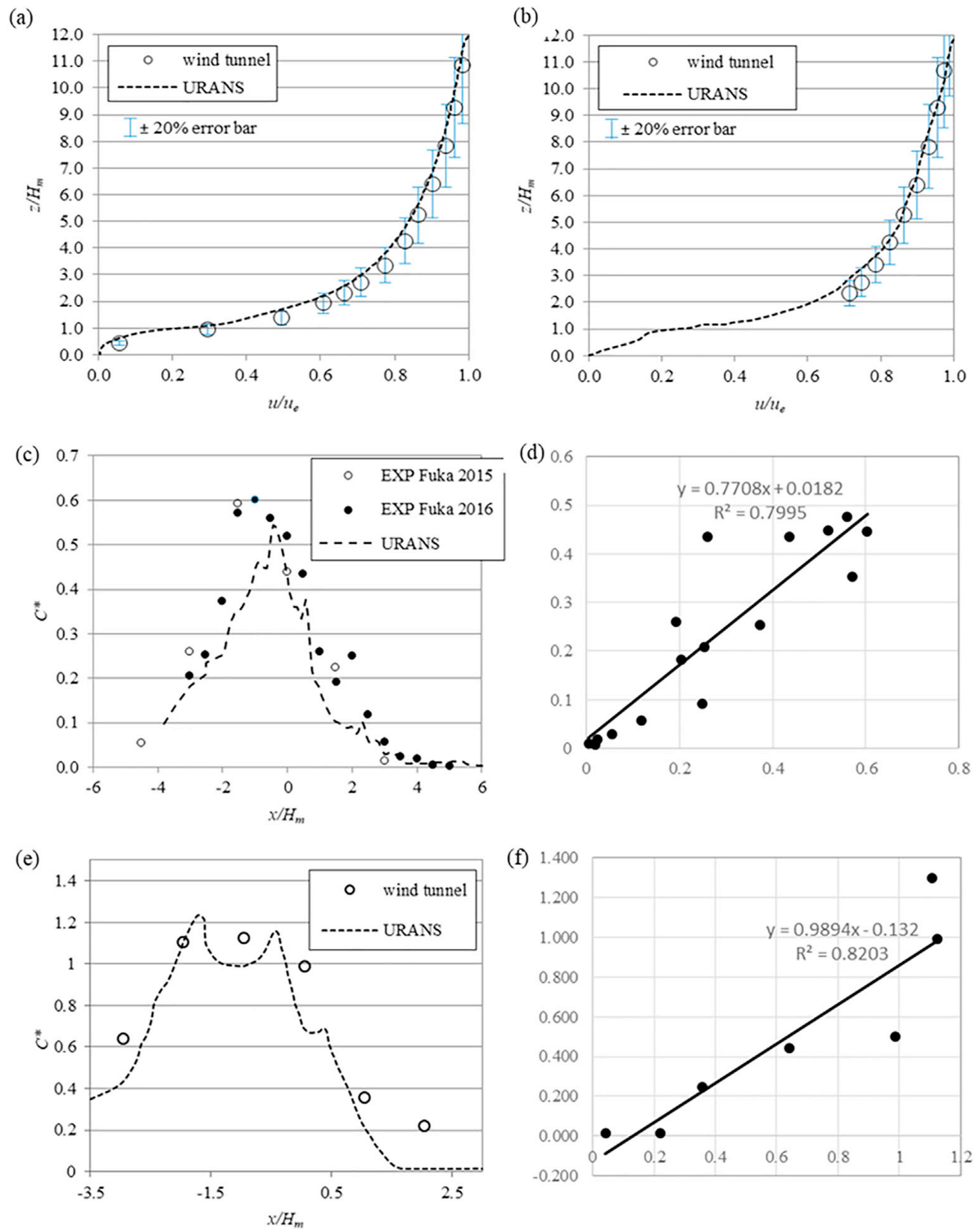

Fig. 6. (2 column) – Measured and simulated normalized mean velocity profiles of at $x = 0.5H$ and y = 0.0–12H (a) 0° and (b) 90° wind direction. Measured and simulated normalized mean concentration profiles at $z = 0.5H$ and x = 0.0 (c) 0° and (e) 90° wind direction. Scatter plot of normalized pollutant concentration between the measured and simulated data at (d) 0° and (f) 90°.

CFD validation results of wind velocity profiles. Fig. 6 (a, b) shows that the vertical variation of the horizontal velocity component for both wind directions (0° and 90°) presented a deviation smaller than 20%, indicating a good precision range.

Fig. 6(c–f) shows the validation results for the mean concentration profiles. For the mean concentration profiles, although for the 0° wind direction the maximum values are slightly underestimated (Fig. 6c) the URANS results were able to reproduce the concentration distribution pattern. The scatter plot illustrated in Fig. 6c, e shows that the two sets of data (measured and simulated) are positively correlated, with a correlation value of approximately 0.8 for both wind directions (0° and 90°).

In addition to the correlation value, the normalized mean squared error (NMSE) is used to quantify the agreement between the measured and the simulation results for pollutant concentration. The NMSE is indicated by COST (Schatzmann et al., 2010) to evaluate the validation results of CFD simulations for a parameter that has only positive or negative values. This metric used for this purpose is also presented in Herring and Huq (2018) and used in An et al. (2019). NMSE is strongly influenced by infrequently occurring high observations and predictions for the concentrations and indicates both, systematic and random errors (Schatzmann et al., 2010). For an ideal model prediction, the NMSE would be equal to zero. However previous studies suggested the judgment criteria for this metric for pollutant concentration could be smaller than four (Hanna et al., 2004; Herring and Huq, 2018; Schatzmann et al., 2010). In this study, an NMSE value of approximately 0.1 is obtained, which can be considered a satisfactory model performance. This implies that the model is capable of predicting the pollutant concentration robustly. In agreement with other studies (An et al., 2019a; Lee, 2017; Yuan et al., 2019c) the SST k-ω model is identified as a good tool for modelling air pollutant dispersion, providing acceptable accuracy and reasonable computational cost.

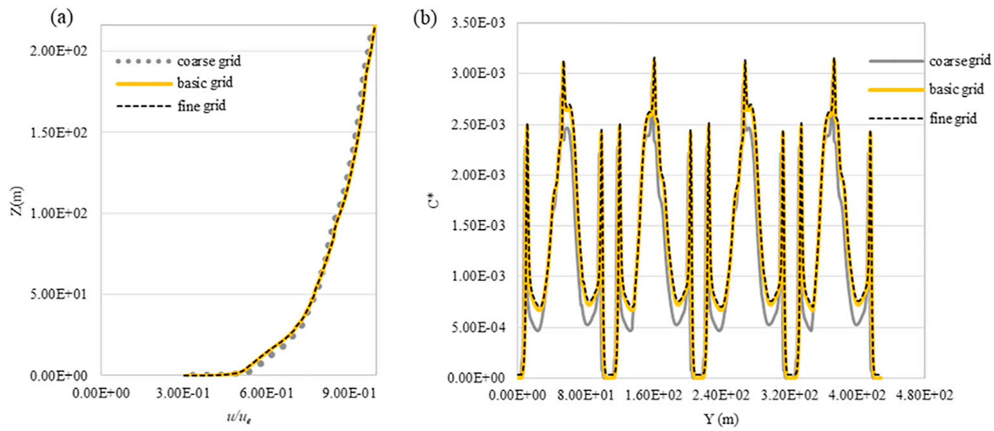

Fig. 7. (2 column) – (a) Normalized mean velocity profiles at 0° wind direction and (b) Normalized mean concentration at 2m height in the domain middle; under different types of grids.

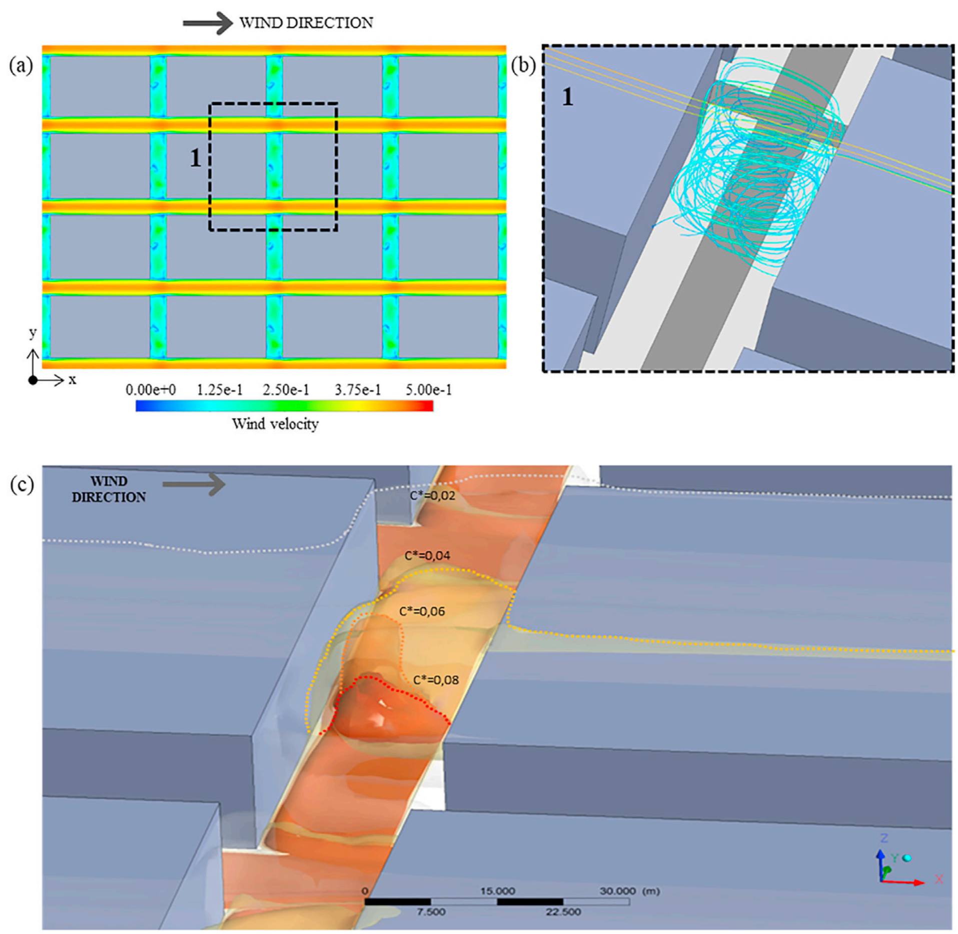

Fig. 8. (2 column) – (a) Normalized mean velocity magnitude on horizontal plane ($z = 2$m); (b) Velocity streamline between blocks. (c) Mean concentration isosurface for c* = 0.2; c* = 0.04; c* = 0.06; c* = 0.08.

3.2. Grid sensitivity analysis

The single-block typology was selected as the reference case; the scale of the block geometries and mesh grid amounts for the other four typologies investigated are within the same magnitude order. Fig. 7 shows the results for the grid sensitivity analysis. The mesh independence was investigated using three different mesh sizes: a coarse grid (2,600,000 elements), a base grid (4,000,000 elements), and a fine grid (6,000,000). The variables analyzed are the normalized pollutant concentration from a line in the domain middle at 2 m height and the vertical profile of the normalized wind velocity in the center of the domain. That is a satisfying correspondence between the basic and the fine mesh, indicating a good mesh independence behavior and validating the basic grid as appropriate in this study.

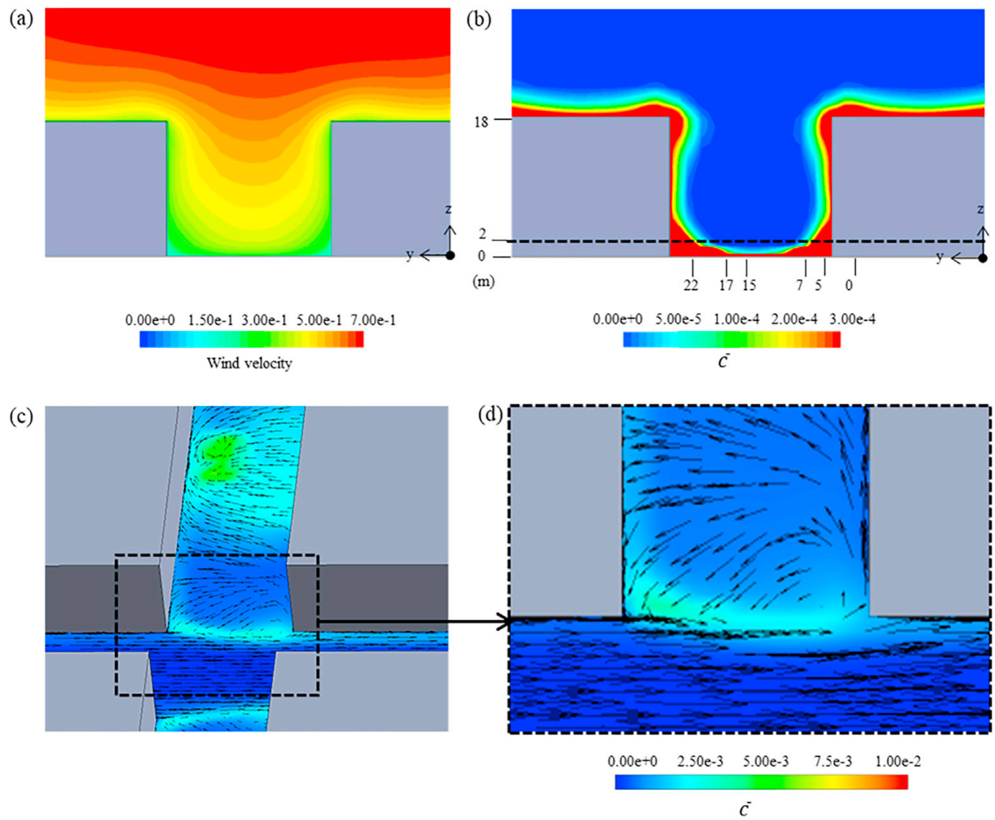

Fig. 9. (2 columns) – Parallel canyon vertical Section (a) Normalized mean concentration and (b) Normalized mean velocity magnitude; (c) Normalized mean concentration and velocity vector on the horizontal plane ($z = 2$m) and (d) Amplified cross-section zone.

4. Results and discussions

4.1. Analysis of ventilation and pollutant concentration: single-block typology (case base)

The single-block typology was chosen as the reference case due to its simpler geometry. The key phenomena involved in the fluid flow that affects the pollutant dispersion process are: channeling (Fig. 8a), recirculation (Fig. 8b), and turbulent diffusion (Fig. 8c). The canyons parallel to the air flow direction form symmetric long streets having a channeling effect. This effect is enhanced by the contiguous geometry of buildings facades on both street sides. The air flow channeling is responsible for bigger wind velocity in parallel canyons. In contrast, the perpendicular canyons have lower wind speeds. The recirculation occurs especially between the blocks in the x-axis direction, and on the road intersection. It can be observed that the recirculation in the central of the perpendicular canyon transports pollutants of the ground to the buildings' roof downstream and, therefore, out of the urban canopy (Fig. 8c). The velocity gradients in this region produce considerable levels of turbulence, which causes transport by turbulent diffusion of pollutants out of the canopy. In fact, these are the main mechanisms of pollutant's exfiltration from the canopy interior to the free atmosphere (Goulart et al., 2019), contributing to "cleansing" the air in the urban region.

For the parallel canyon Fig. 9a and b presents the normalized mean concentration and the mean velocity magnitude. The pollutant accumulates near the ground and building surfaces. This accumulation occurs near the walls bordering region where the air flow velocity is low. Oppositely, at the canyon center, away from the pedestrian pathway, the concentration decreases, as air flow velocity increases. When the wind is parallel to the street axis, the concentrations on both sides of the canyon become equal, corroborative with the results of Vardoulakis et al. (2003). In the horizontal plane, at the road intersection, the channeled flow from

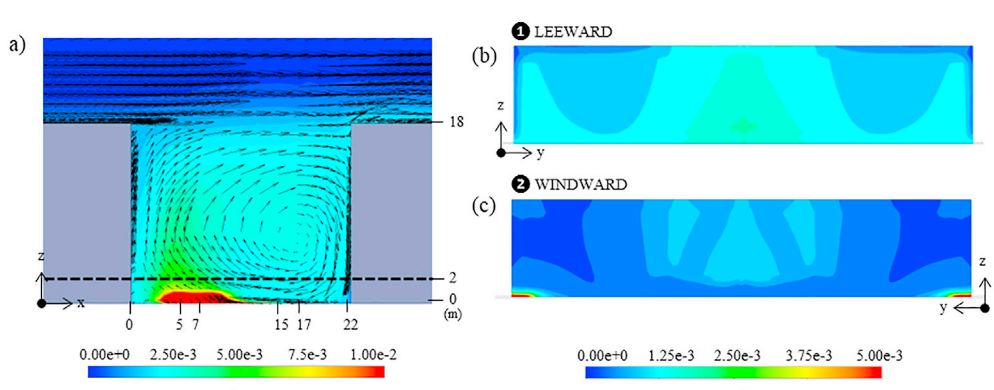

Fig. 10. (2 columns) – (a) Normalized mean concentration with velocity vector at vertical section; and Normalized mean concentration at (c) Leeward facade and (d) Windward facade.

Table 3
(2 column) Description of facades contiguity and canyons aspect ratio for the five typologies.

Typology	Parallel Canyon			Perpendicular Canyon		
	Contiguity (L)	H/W	W (m)	Contiguity (L)	H/W	W (m)
Single-block	Continuous facades 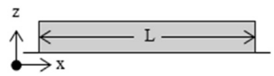 L = 131 m	0.8	22	Continuous facades 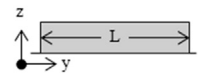 L = 85m	0.8	22
Detached Buildings	Permeable facades 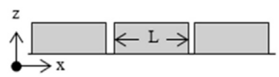 L = 43 m	1	18	Permeable facades 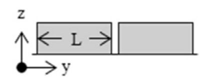 L = 43m	1	18
Central Courtyard	Continuous facades 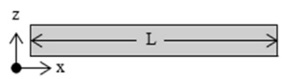 L = 141 m	1.5	12	Continuous facades 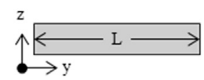 L = 95m	1.5	12
Inner Courtyards	Continuous facades 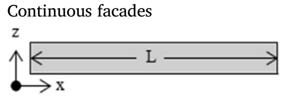 L = 141 m	1.5	12	Continuous facades 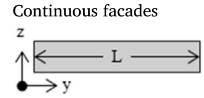 L = 95m	1.5	12
Row	Continuous facades 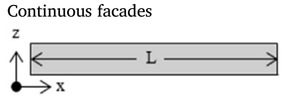 L = 141 m	0.8	22	Permeable facades 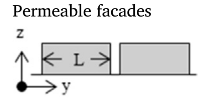 L = 40m	1.5	12

Legend: H/W – Canyon aspect ratio; W – Canyon width, which is the sum of street width, pedestrian pathway, and building setbacks.

the parallel streets interacts with the recirculatory movement in the perpendicular canyons and with the buildings' corners (Fig. 9c and d). The air flow around the corner creates a vortex towards the adjacent street, interacting with the recirculation vortex in the center of the perpendicular streets, causing the pollutant concentration in the intersection region. The central of perpendicular streets displays a symmetric swirling movement in the horizontal axis. In the central area of the block, downstream of the buildings occurs a stagnation point, which has the lowest air flow velocity and the highest accumulation of pollutants.

Fig. 10a exhibits, for the perpendicular canyon, the normalized mean concentration and the velocity vector on the vertical plane. Larger concentration values occur at the pedestrian pathway under 2 m height close to the leeward building. It can be observed that the concentration values below 2 m are significantly higher for the perpendicular canyons in comparison with the parallel canyons, with values exceeding 1 order of magnitude for the perpendicular canyons (Figs. 9b and 10a). Fig. 10a on the vertical plane, the perpendicular air flow forms a vortex between buildings and an ascendant flux. The vortex formed cause concentration to accumulate near the leeward facade.

The normalized mean concentration on buildings facades is displayed in Fig. 10b–c. Higher values of concentration are found on the leeward facade than on the windward wall. The recirculation zone between buildings carries the pollutant to the leeward facade, which presents a symmetrical concentration pattern (Fig. 10b). On the windward facade, the descending flow near the buildings assists the dispersion process causing the concentration to accumulate in the lower corner close to the source (Fig. 10d), nonetheless, concentration is a little higher at the façade's center. Additionally, the vortex at crossroad sections produces lower wind speeds in this region which reinforces the accumulation point on the windward facade. As observed, on perpendicular canyons at the pedestrian height, the higher concentration values occur on the leeward.

4.2. Analysis of urban block typologies ventilation and pollutant concentration

Several studies (An et al., 2019a; Yang et al., 2019b) point out that the urban block arrangement is one of the most important factors for pollutant dispersion in the urban environment. To understand the impact of urban block typologies in pollutant concentration, five real-like urban configurations were investigated: single-block; the detached buildings; the central courtyard; the inner courtyards; and the row. All the configurations present the same building volume (*FAR*), surface coverage (*SC*) (i.e., same porosity). Even though the five urban block typologies present the same urban metrics, the arrangement of the buildings represents a distinct location of the area not occupied by the buildings (free area) into the block. For the courtyard typologies, all the free area is allocated in the center of the block. On the other hand, for the single-block typology, all the free area is distributed around a single building, increasing the effective width of the street canyons. For the detached buildings and row typologies, the free area of the block is allocated between buildings. This feature leads to two main differences between the typologies: (i) facades contiguity and (ii) canyon aspect ratio (*H/W*). Regarding the facades contiguity, the urban block typologies can be described as contiguous (no openings) or permeable (with openings). For all five typologies, the aspect ratio for parallel and perpendicular canyons varies from 0.8 to 1.5, considered a regular canyon according to Oke (1988). Table 3 presents the descriptions of these parameters for the five typologies.

Fig. 11 displays the normalized mean velocity magnitude at the pedestrian level, for the five urban typologies on the horizontal plane (2m height). In this case, the wind direction is perpendicular to the shorter building wall, creating an obstacle to the air flow. The canyons perpendicular to wind direction presents low wind velocity. Meanwhile, the streets parallel to wind direction channeling the air flow. In the single-block case, the larger street width tends to reduce the resistance to the fluid flow in the street canyons, increasing ventilation (Fig. 11a). For the detached buildings and row typologies (Fig. 11b,e), the free area between buildings improves the air flow within each block. However, this free area distribution also tends to reduce the width of the canyon increasing the resistance to the air flow, decreasing street ventilation in comparison with the single-block typology. For the courtyard cases (Fig. 11c and d), the unbuilt area inside the urban block behaves as a wind velocity reducer.

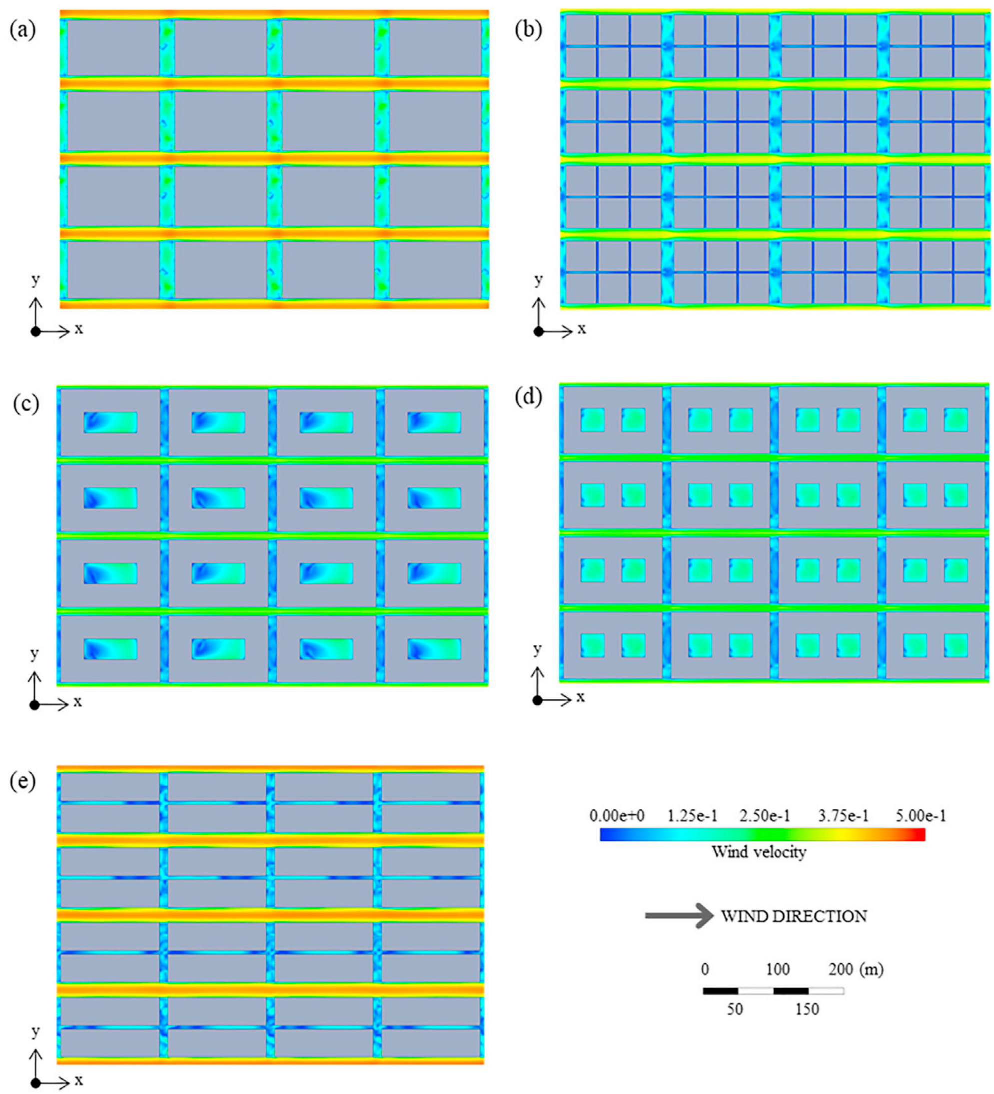

Fig. 11. (2 column) - Normalized mean velocity magnitude for 5 urban block typologies at 2m height; (a) Single-block; (b) Detached buildings; (c) Central courtyard; (d) Inner courtyards; (e) Row.

Fig. 12 displays the normalized mean concentration at the pedestrian level, for the five typologies. Given the symmetrical domain configuration, the concentration at the streets presents a trend. In real urban areas, the number of blocks in a row can be more than four. In that sense, it is important to note that the current simulation setup enables the simulation of a fully developed fluid flow inside the canopy, but does not allow the complete development of the concentration fields, since there is not sufficient distance for that. To obtain fully developed concentration fields the computational domains required would be significantly longer and, therefore, requiring a prohibitively larger computational cost. As a consequence, the results presented here are intended to analyze the effects of the fluid flow characteristics upon the ventilation and dispersion capacity of each typology under similar conditions.

For all five studied cases, the pollutant accumulates more considerably in perpendicular canyons, especially in the urban block central region along the leeward facades. Meanwhile, the canyons parallel to the wind direction presents the lowest concentration in this region for all the cases. The channeling flow improves the pollutant flush. As a result, the cases that presented higher wind velocities display lower concentrations. Therefore, the largest concentration is registered for the detached building's typology (Fig. 12b), follow by both courtyard typologies (Fig. 12c and d); on the other hand, the lowest concentration is registered for the single-block typology (Fig. 12a) and the row typology (Fig. 12e). Moreover, for each case, the level of facades' contiguity or permeability affects the air flow and consequently the pollutant concentration. For the total plane area, the case of the detached buildings presents a pollutant concentration of 80% larger than the single-block case (Fig. 12f). In the detached building's typology, concentration increases with the downstream distance which is less evident for the other typologies. The unbuilt area between buildings in this case appears in both along wind and crosswind directions. The unbuilt area between the buildings for this case is displayed both in the along wind and crosswind directions. This arrangement creates a weak flow throughout the middle of the block carrying the pollutant from one street to the next one contributing to an increased pollutant accumulation at the downwind locations.

For the contiguous facades, at the parallel canyons, the courtyard typologies (central and inner) present lower wind velocity and larger pollutant accumulation compared to the single-block and the row typology. It can be seen that the block's unbuilt area (i.e. the courtyards) remains “clean”, with a low level of pollutant concentration. Kurppa et al. (2018) identified that courtyards tend to remain clean, which implies that, in general, traffic-related pollutants are not easily transported to these inside areas. In these cases, free spaces do not contribute to better air circulation, but function as “sheltered” and relatively pollution-free regions. In agreement with the results of Shen et al. (2017), the greater facades' continuity contributes to a greater wind channeling and less

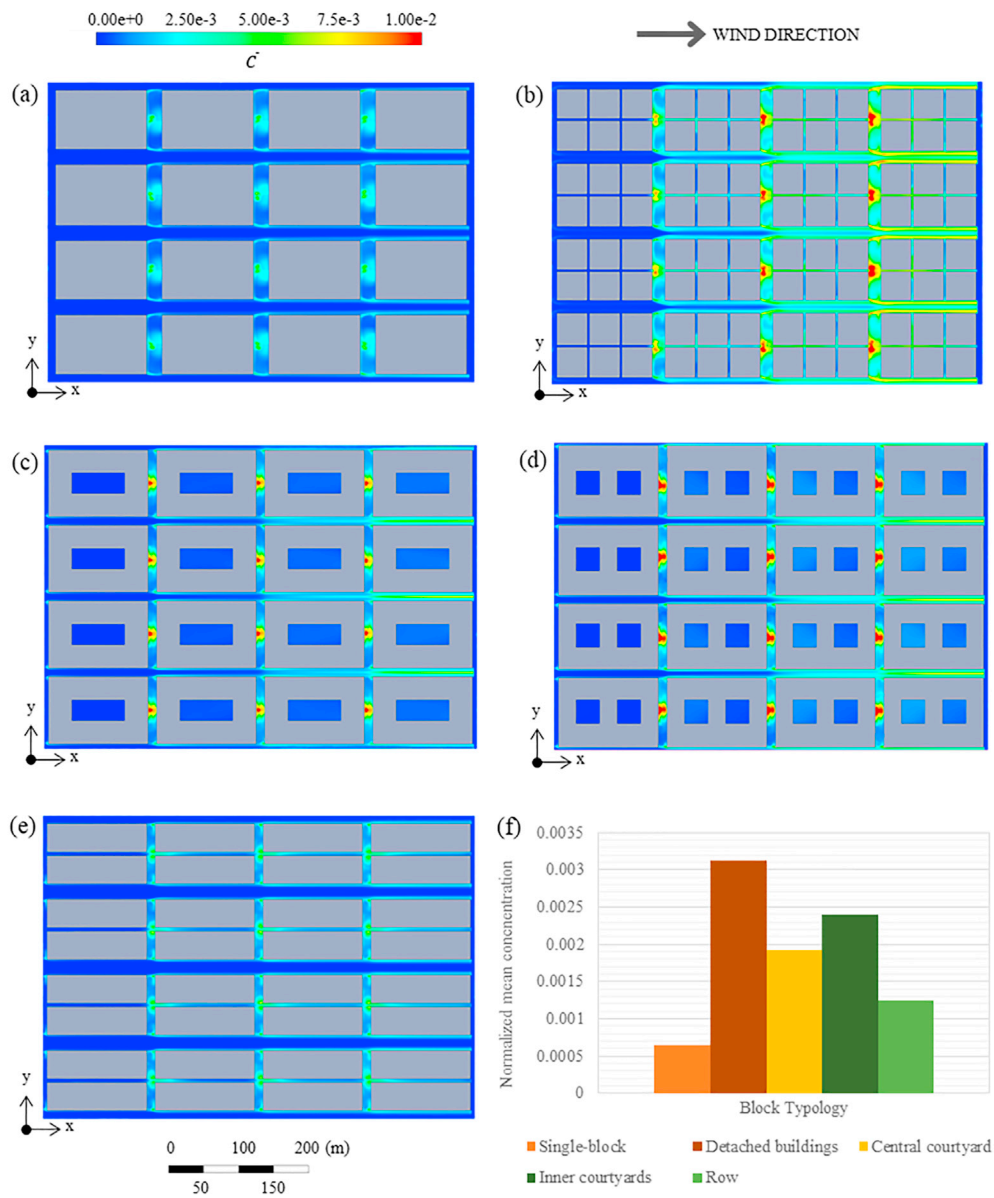

Fig. 12. (2 column) - Normalized mean concentration for 5 urban block typologies on the horizontal plane at 2m high; (a) Single-block; (b) Detached buildings; (c) Central courtyard; (d) Inner courtyards; (e) Row; and Normalized mean concentration values on the horizontal plane on 2 m height for (f) The five urban block typologies: single-block; detached buildings; central courtyard; inner courtyards; row.

concentration in this region. Consequently the larger the number of facades opening, the larger the tendency of disruption of the main flow.

The five typologies display diverse arrangements of the building into the block, which influences the street width (W) resulting in different aspect ratios (H/W). In parallel canyons, the aspect ratio influences the channeling effect. Meanwhile, in perpendicular canyons, the aspect ratio influences the vortex formation. According to Oke (1988), the aspect ratio of these typologies can all be classified as the skimming flow regime, which is characterized by the formation of a single vortex within the canyon. Fig. 13 shows the normalized mean concentration in the vertical section for parallel and perpendicular canyons for the five cases. The greatest concentration for all typologies is registered at the pedestrian level, especially on the sidewalks.

For the parallel canyon, the courtyard cases present the highest aspect ratio ($H/W = 1.5$), followed by the detached buildings ($H/W = 1$), and the single-block and the row cases ($H/W = 0.8$). Furthermore, for the perpendicular canyon, the courtyard cases and the row case present the highest aspect ratio ($H/W = 1.5$), followed by the detached buildings ($H/W = 1$), and the single-block ($H/W = 0.8$). For parallel canyons, Soulhac and Salizzoni (2010) have shown that concentration increases as the street canyon is narrower (higher aspect ratio). Further, for the perpendicular canyons, it has been shown in several studies (Fu et al., 2017; He et al., 2017; Shen et al., 2017a) that a higher aspect ratio presents higher pollutant concentrations. However, in the present study, this effect was not so linear neither on parallel nor in perpendicular canyons. The result indicates that for contiguous facades a higher aspect ratio represents higher pollutant accumulation. Nonetheless, this assumption cannot be inferred to permeable facades. Therefore, the aspect ratio alone is not enough to analyze street ventilation and consequently pollutant dispersion.

Despite the aspect ratio for the parallel canyons, all five cases present a symmetric concentration pattern. Different from the parallel canyons, the vorticity in perpendicular streets modifies the concentration behavior. The level of contiguity on the facades parallel to wind direction proved to be an influencing factor in pollutant concentration. Moreover, the level of contiguity on the facades perpendicular to wind direction also

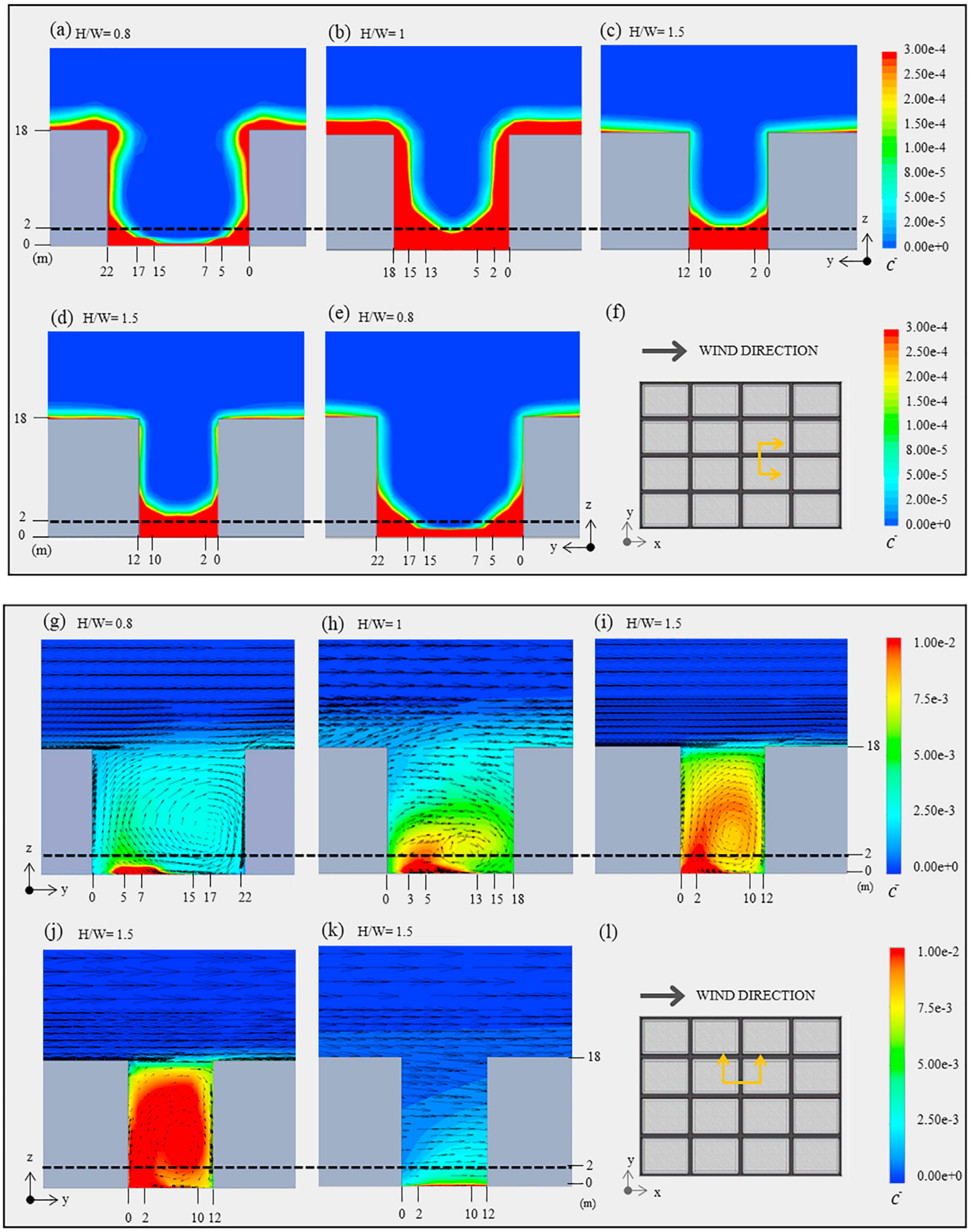

Fig. 13. (2 column) – Normalized mean concentration for the five typologies: (a) Single-block; (b) Detached buildings; (c) Central courtyard; (d) Inner courtyards; (e) Row; (f) Parallel canyon vertical section; Normalized mean concentration with velocity vector at vertical plane and aspect ratio (H/W) for the five typologies: (g) Single-block; (h) Detached buildings; (i) Central courtyard; (j) Inner courtyards; (k) Row; Located on (l) Perpendicular canyon.

impacts pollutant concentration. For example, a single vortex formation is found in cases with contiguous facades (single block and courtyard cases, Fig. 13g, i, j), but not in the cases of permeable facades (detached buildings and the row cases, Fig. 13h,j). For instance, on both permeable facades configurations, the air flow in the opening is sufficiently intense to transport the pollutants from one perpendicular street to the next. Nonetheless, the larger opening on the row case enables larger flow velocities, channeling the wind through the block. While in the detached typology, the opening gap is not large enough to enable large velocities, and so the inertia of the flow is not sufficient to completely suppress the recirculation zone in front of the gap.

Moreover, the level of contiguity on leeward facades also impact the concentration distribution on buildings' wall, as can been seen in Fig. 14. In most cases, the largest concentration occurs in the central region of the block and presents a symmetrical distribution about the vertical axis. The cases with contiguous leeward facades, single-block (Fig. 14a), and courtyard cases (Fig. 14c and d) display a similar concentration pattern. However, higher pollutant concentrations can be seen in the inner courtyards typology. The main difference between the courtyard cases is the courtyard aspect ratio, i.e., central courtyard (courtyard $H/W = 0.24$), inner courtyard (courtyard $H/W = 0.5$). Gronemeier and Sühring (2019) have identified that a higher courtyard aspect ratio represents higher concentration inside the courtyard. For the present study, it was found that the courtyard aspect ratio also impacts the outside regions. Although the permeable facades cases, detached buildings (Fig. 14b), and the row (Fig. 14e) do not present the lowest average concentrations at pedestrian height, it is observed that the maximum concentrations of pollutants on the buildings' facades are significantly lower than for

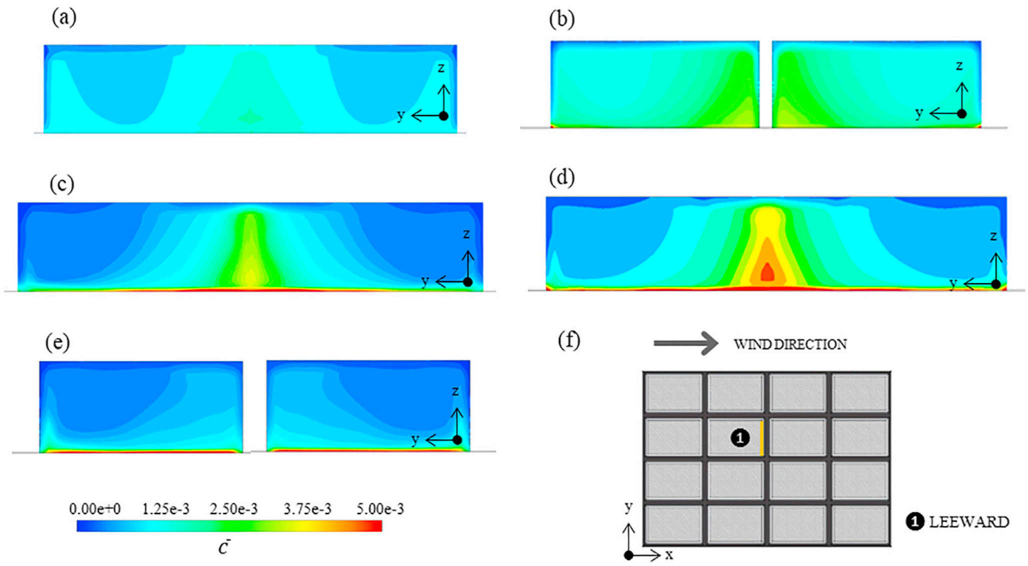

Fig. 14. (2 column) – Normalized mean concentration at leeward facades in the five typologies: (a) Single-block; (b) Detached buildings; (c) Central courtyard; (d) Inner courtyards; (e) Row; (f) Location of the leeward facade.

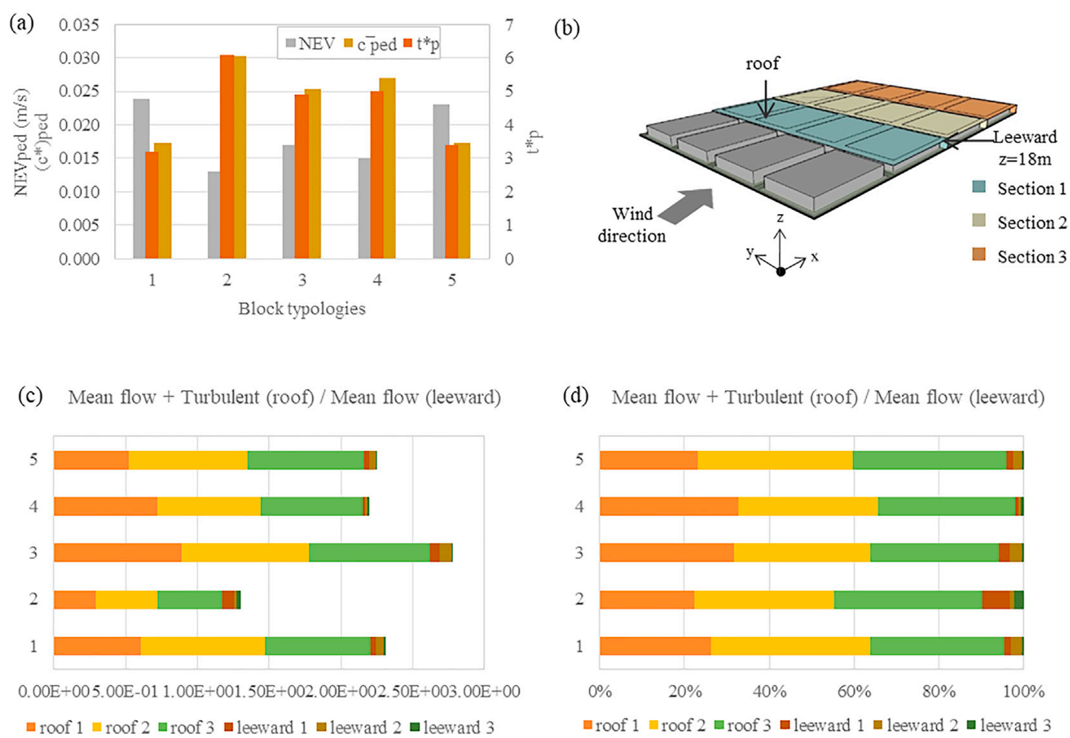

Fig. 15. (2 columns) – (a) $\bar{\tau}_p^*$, *NEV*, $(\bar{c})ped$ for each typology in the entire pedestrian volume (1-5: sequentially, single-block, detached buildings, central courtyard, inner courtyards, row). (b) Illustration of different sections. (c) Mean convective and turbulent fluxes out of the canopy (roof) and mean convective flux through the leeward boundaries that represent the pollutant removal contribution of horizontal and vertical flows for each typology. (d) Mean convective and turbulent fluxes out of the canopy and mean convective flow through the leeward boundaries for each typology in percentage.

configurations without openings in the middle of perpendicular canyons.

4.3. Breathability and ventilation efficiency assessment

The city breathability is evaluated using the mean age of air to understand the ventilation potential of different building configurations (block typologies). This potential is directly related to the air flow patterns which means that pollutant removal is linked to convective and turbulent flow directly. Fig. 15a shows for the entire pedestrian volume the mean age of air ($\bar{\tau}_p^*$), *NEV* and c_{ped} for the five block typologies. As expected, $\bar{\tau}_p^*$ and c_{ped} present similar distributions. As mentioned before, $\bar{\tau}_p^*$ is the typical time for the pollutant to be washed out by an air flow system. Consequently, the lower $\bar{\tau}_p^*$, the higher the ventilation will be. Therefore, the cases with the highest NEV values exhibit a lower $\bar{\tau}_p^*$ and c_{ped}. The net escape velocity increases with the channeling effect, as also identified by Peng et al. (2019). The detached buildings case had the lowest NEV value, which means that the small spaces between buildings are not enough to increase the pollutant removal.

The highest mean age of air value was found in the case of the detached buildings followed by the inner courtyards, central courtyard, row, and single-block. The detached building presents a $\overline{\tau}_p^*$ about 50% larger than the single-block case. The single-block and the row case had a similar performance. The courtyard cases also had similar performance and displayed $\overline{\tau}_p^*$ 36% larger than the single-block case. However, it is interesting to note that the mean age of air in the courtyard cases is only 20% smaller than in the case of the detached buildings. Considering that inside the courtyards there is little pollutant accumulation, this means that there is a larger accumulation on the streets and sidewalks. Comparing to the literature results, for an idealized building array with the same surface coverage (80%), An et al. (2019) found a difference of 45% for pollutant accumulation for different buildings arrangement. For real canyons, Shen et al. (2017) observed a difference of 25% for different cities (i.e. different facades' contiguity). Therefore, it is significant to note that in the present study, variations in the investigated arrangement of buildings can impact the mean age of air by up to 50%.

To understand the pollutant removal contribution of horizontal and vertical flows for each typology, three sections on the domain were delimited as depicted in Fig. 15b. Fig. 15 shows the mean convective flow at the leeward boundaries (horizontal fluxes) and the mean convective and turbulent flows out of the canopy (vertical fluxes). In Fig. 14c–d, it can be seen that for the five typologies, pollutant transport mainly occurs due to the vertical flow through the top of the canopy. As already mentioned, the five cases can be classified into the skimming flow regime. In this regime, the vertical transport of pollutants is dominated by the turbulent component in agreement with the results found here. In the single-block typology, which presents less pollutant concentration in the pedestrian volume, the vertical transport of pollutants through the top of the canopy is higher than in the other cases. Conversely, the case with higher pollutant concentration, which is the case of the detached buildings, displays lower vertical fluxes. Thereupon, the permeable facades on both wind directions reduce the vertical mean turbulent flow in the street roofs.

5. Conclusions and discussions

Five urban block typologies with fixed values of *FAR* (5), *SC* (80%), and *H* (18m) were investigated. These typologies represent a diverse arrangement of the buildings into the urban block leads to a different level of contiguity on facades and different canyon aspect ratio, which implicates distinctive pollutant concentration. The main findings are summarized as follows.

Concerning the facade's level of contiguity and canyon aspect ratio:

- The correlation between aspect ratio and concentration was not exactly linear as the level of facade's contiguity impacts this correlation.
- On parallel canyon, the contiguous facade associated with the lower aspect ratio improves the channeling effect and reduces the pollutant concentration.
- Despite the contiguous facades in the courtyard cases, the unbuilt area inside the urban block acts as a wind velocity reducer.
- For contiguous facades in parallel and perpendicular canyons, a higher aspect ratio promotes more pollutant accumulation.
- For permeable facades on both canyon direction, the openings' location impacts concentration. The openings in the alongwind direction channeled the wind throughout the blocks. While the crosswind openings softened the channeling effect increasing pollutant concentration.

Concerning the ventilation indices:

- The channeling effect improves the net escape velocity and reduces pollutant concentration.
- Narrower openings in the crosswind direction can increase the mean age of air up to 50%.
- The courtyard area represents a cleaner space into the block, however, pollutant concentration is higher on streets and sidewalks.
- The flows are dominated by the vertical mean convective and turbulent flows at the top of the urban canopy.
- Permeable facades help to reduce the vertical mean turbulent flow at the roof level.

Finally, it is important to stress that real cities' morphologies are diverse and complex. Further studies could investigate the influence of building height variability, other wind directions, and a diversity of FAR and SC values.

CRediT authorship contribution statement

Fabiana Trindade da Silva: Conceptualization, Methodology, Validation, Formal analysis, Investigation, Writing - original draft, Writing - review & editing, Visualization. **Neyval Costa Reis:** Conceptualization, Methodology, Validation, Formal analysis, Resources, Writing - review & editing, Supervision. **Jane Meri Santos:** Conceptualization, Methodology, Formal analysis, Resources, Writing - review & editing. **Elisa Valentim Goulart:** Conceptualization, Methodology, Validation, Formal analysis, Writing - review & editing. **Cristina Engel de Alvarez:** Conceptualization, Methodology, Formal analysis, Writing - review & editing, Supervision.

Declaration of competing interest

The authors declare that they have no known competing financial interests or personal relationships that could have appeared to influence the work reported in this paper.

Acknowledgment

The authors wish to thank the Coordenação de Aperfeiçoamento de Pessoal de Nível Superior – Brasil (CAPES) and the Fundação de Amparo à Pesquisa e Inovação do Espírito Santo - Brasil (FAPES) for its financial support.

References

An, K., Wong, S.M., Fung, J.C.H., 2019a. Exploration of sustainable building morphologies for effective passive pollutant dispersion within compact urban environments. Build. Environ. 148, 508–523. https://doi.org/10.1016/j.buildenv.2018.11.030.

An, K., Wong, S.M., Fung, J.C.H., 2019b. Exploration of sustainable building morphologies for effective passive pollutant dispersion within compact urban environments. Build. Environ. 148, 508–523. https://doi.org/10.1016/j.buildenv.2018.11.030.

ANSYS Academic Research, 2018. ANSYS Fluent Theory Guide. In: ANSYS Help System.

Ayo, S.A., Mohd-Ghazali, N., Mansor, S., 2015. Outdoor ventilation performance of various configurations of a layout of two adjacent buildings under isothermal conditions. Build. Simul. https://doi.org/10.1007/s12273-014-0195-2.

Bady, M., Kato, S., Huang, H., 2008. Towards the application of indoor ventilation efficiency indices to evaluate the air quality of urban areas. Build. Environ. 43, 1991–2004. https://doi.org/10.1016/j.buildenv.2007.11.013.

Blocken, B., 2015. Computational Fluid Dynamics for urban physics: importance, scales, possibilities, limitations and ten tips and tricks towards accurate and reliable simulations. Build. Environ. 91, 219–245. https://doi.org/10.1016/j.buildenv.2015.02.015.

Blocken, B., 2014. 50 years of computational wind engineering: past, present and future. J. Wind Eng. Ind. Aerod. https://doi.org/10.1016/j.jweia.2014.03.008.

Brunekreef, B., Holgate, S.T., 2002. Air pollution and health. Lancet 360, 1233–1242. https://doi.org/10.1016/S0140-6736(02)11274-8.

Buccolieri, R., Salizzoni, P., Soulhac, L., Garbero, V., Di Sabatino, S., 2015. The breathability of compact cities. Urban Clim. 13, 73–93. https://doi.org/10.1016/j.uclim.2015.06.002.

Carpentieri, M., Robins, A.G., 2015a. Influence of urban morphology on air flow over building arrays. J. Wind Eng. Ind. Aerod. https://doi.org/10.1016/j.jweia.2015.06.001.

Carpentieri, M., Robins, A.G., 2015b. Influence of urban morphology on air flow over building arrays. J. Wind Eng. Ind. Aerod. 145, 61–74. https://doi.org/10.1016/j.jweia.2015.06.001.

Carpentieri, M., Robins, A.G., 2015c. Influence of urban morphology on air flow over building arrays. J. Wind Eng. Ind. Aerod. 145, 61–74. https://doi.org/10.1016/j.jweia.2015.06.001.

Castro, I.P., Xie, Z.T., Fuka, V., Robins, A.G., Carpentieri, M., Hayden, P., Hertwig, D., Coceal, O., 2017. Measurements and computations of flow in an urban street system. Boundary-Layer Meteorol. 162, 207–230. https://doi.org/10.1007/s10546-016-0200-7.

Chen, L., Hang, J., Sandberg, M., Claesson, L., Di Sabatino, S., 2017a. The influence of building packing densities on flow adjustment and city breathability in urban-like geometries. Procedia Eng. 198, 758–769. https://doi.org/10.1016/j.proeng.2017.07.127.

Chen, L., Hang, J., Sandberg, M., Claesson, L., Di Sabatino, S., Wigo, H., 2017b. The impacts of building height variations and building packing densities on flow adjustment and city breathability in idealized urban models. Build. Environ. 118, 344–361. https://doi.org/10.1016/j.buildenv.2017.03.042.

Cheshmehzangi, A., Butters, C., 2016. Sustainable living and urban density: the choices are wide open. Energy Procedia 88, 63–70. https://doi.org/10.1016/j.egypro.2016.06.020.

Ferziger, J.H., Perić, M., 2002. Computational methods for fluid dynamics, computational methods for fluid dynamics. https://doi.org/10.1007/978-3-642-56026-2.

Franke, J., Hellsten, A., Schlünzen, H., Carissimo, B., 2007. Best Practice Guideline for the CFD Simulation of Flows in the Urban Environment. COST action.

Fu, X., Liu, J., Ban-Weiss, G.A., Zhang, J., Huang, X., Ouyang, B., Popoola, O., Tao, S., 2017. Effects of canyon geometry on the distribution of traffic-related air pollution in a large urban area: implications of a multi-canyon air pollution dispersion model. Atmos. Environ. 165, 111–121. https://doi.org/10.1016/j.atmosenv.2017.06.031.

Fuka, V., Xie, Z.T., Castro, I.P., Hayden, P., Carpentieri, M., Robins, A.G., 2018. Scalar fluxes near a tall building in an aligned array of rectangular buildings. Boundary-Layer Meteorol. 167, 53–76. https://doi.org/10.1007/s10546-017-0308-4.

Gehl, J., Svarre, B., 2013. How to study public life, how to study public life. https://doi.org/10.5822/978-1-61091-525-0.

Goulart, E.V., Reis, N.C., Lavor, V.F., Castro, I.P., Santos, J.M., Xie, Z.T., 2019. Local and non-local effects of building arrangements on pollutant fluxes within the urban canopy. Build. Environ. 147, 23–34. https://doi.org/10.1016/j.buildenv.2018.09.023.

Gronemeier, T., Sühring, M., 2019. On the effects of lateral openings on courtyard ventilation and pollution-A large-eddy simulation study. Atmosphere (Basel) 10. https://doi.org/10.3390/atmos10020063.

Guo, F., Zhu, P., Wang, S., Duan, D., Jin, Y., 2017. Improving natural ventilation performance in a high-density urban district: a building morphology method. Procedia Eng. 205, 952–958. https://doi.org/10.1016/j.proeng.2017.10.149.

Hang, J., Chen, L., Lin, Y., Buccolieri, R., Lin, B., 2018. The impact of semi-open settings on ventilation in idealized building arrays. Urban Clim. 25, 196–217. https://doi.org/10.1016/j.uclim.2018.07.003.

Hang, J., Li, Y., Sandberg, M., Buccolieri, R., Di Sabatino, S., 2012. The influence of building height variability on pollutant dispersion and pedestrian ventilation in idealized high-rise urban areas. Build. Environ. 56, 346–360. https://doi.org/10.1016/j.buildenv.2012.03.023.

Hang, J., Wang, Q., Chen, X., Sandberg, M., Zhu, W., Buccolieri, R., Di Sabatino, S., 2015. City breathability in medium density urban-like geometries evaluated through the pollutant transport rate and the net escape velocity. Build. Environ. 94, 166–182. https://doi.org/10.1016/j.buildenv.2015.08.002.

Hanna, S.R., Hansen, O.R., Dharmavaram, S., 2004. FLACS CFD air quality model performance evaluation with Kit Fox, MUST, Prairie Grass, and EMU observations. Atmos. Environ. https://doi.org/10.1016/j.atmosenv.2004.05.041.

He, L., Hang, J., Wang, X., Lin, B., Li, X., Lan, G., 2017. Numerical investigations of flow and passive pollutant exposure in high-rise deep street canyons with various street aspect ratios and viaduct settings. Sci. Total Environ. 584 (585), 189–206. https://doi.org/10.1016/j.scitotenv.2017.01.138.

Herring, S., Huq, P., 2018. A review of methodology for evaluating the performance of atmospheric transport and dispersion models and suggested protocol for providing more informative results. Fluids. https://doi.org/10.3390/fluids3010020.

Iaccarino, G., Ooi, A., Durbin, P.A., Behnia, M., 2003. Reynolds averaged simulation of unsteady separated flow. Int. J. Heat Fluid Flow. https://doi.org/10.1016/S0142-727X(02)00210-2.

Kristóf, G., Füle, P., 2017. Optimization of urban building patterns for pollution removal efficiency by assuming periodic dispersion. J. Wind Eng. Ind. Aerod. 162, 85–95. https://doi.org/10.1016/j.jweia.2017.01.011.

Kurppa, M., Hellsten, A., Auvinen, M., Raasch, S., Vesala, T., Järvi, L., 2018. Ventilation and air quality in city blocks using large-eddy simulation-urban planning perspective. Atmosphere (Basel) 9, 1–27. https://doi.org/10.3390/atmos9020065.

Lee, D.S.H., 2017. Impacts of surrounding building layers in CFD wind simulations. In: Energy Procedia. Elsevier Ltd, pp. 50–55. https://doi.org/10.1016/j.egypro.2017.07.313.

Lin, M., Hang, J., Li, Y., Luo, Z., Sandberg, M., 2014a. Quantitative ventilation assessments of idealized urban canopy layers with various urban layouts and the same building packing density. Build. Environ. 79, 152–167. https://doi.org/10.1016/j.buildenv.2014.05.008.

Lin, M., Hang, J., Li, Y., Luo, Z., Sandberg, M., 2014b. Quantitative Ventilation Assessments of Idealized Urban Canopy Layers with Various Urban Layouts and the Same Building Packing Density, vol. 79, pp. 152–167.

Mannini, C., Šoda, A., Voß, R., Schewe, G., 2010. Unsteady RANS simulations of flow around a bridge section. J. Wind Eng. Ind. Aerod. https://doi.org/10.1016/j.jweia.2010.06.010.

Moonen, P., Dorer, V., Carmeliet, J., 2012. Effect of flow unsteadiness on the mean wind flow pattern in an idealized urban environment. J. Wind Eng. Ind. Aerodyn. 104–106, 389–396. https://doi.org/10.1016/j.jweia.2012.01.007.

Ng, W.Y., Chau, C.K., 2014. A modeling investigation of the impact of street and building configurations on personal air pollutant exposure in isolated deep urban canyons. Sci. Total Environ. 468, 429–448. https://doi.org/10.1016/j.scitotenv.2013.08.077. –469.

Oke, T.R., 1988. Street design and urban canopy layer climate. Energy Build. https://doi.org/10.1016/0378-7788(88)90026-6.

Peng, Y., Gao, Z., Buccolieri, R., Ding, W., 2019a. An investigation of the quantitative correlation between urban morphology parameters and outdoor ventilation efficiency indices. Atmosphere (Basel) 10. https://doi.org/10.3390/atmos10010033.

Peng, Y., Gao, Z., Buccolieri, R., Ding, W., 2019b. An investigation of the quantitative correlation between urban morphology parameters and outdoor ventilation efficiency indices. Atmosphere (Basel) 10, 33. https://doi.org/10.3390/atmos10010033.

Ramponi, R., Blocken, B., de Coo, L.B., Janssen, W.D., 2015. CFD simulation of outdoor ventilation of generic urban configurations with different urban densities and equal and unequal street widths. Build. Environ. 92, 152–166. https://doi.org/10.1016/j.buildenv.2015.04.018.

Ricci, A., Kalkman, I., Blocken, B., Burlando, M., Freda, A., Repetto, M.P., 2017. Local-scale forcing effects on wind flows in an urban environment: impact of geometrical simplifications. J. Wind Eng. Ind. Aerod. https://doi.org/10.1016/j.jweia.2017.08.001.

Schatzmann, M., Olesen, H., Franke, J., 2010. Cost 732 Model Evaluation Case Studies : Approach and Results. COST Action, p. 732.

Sha, C., Wang, X., Lin, Y., Fan, Y., Chen, X., Hang, J., 2018. The impact of urban open space and 'lift-up' building design on building intake fraction and daily pollutant exposure in idealized urban models. Sci. Total Environ. 633, 1314–1328. https://doi.org/10.1016/j.scitotenv.2018.03.194.

Shen, J., Gao, Z., Ding, W., Yu, Y., 2017a. An investigation on the effect of street morphology to ambient air quality using six real-world cases. Atmos. Environ. 164, 85–101. https://doi.org/10.1016/j.atmosenv.2017.05.047.

Shen, J., Gao, Z., Ding, W., Yu, Y., 2017b. An investigation on the effect of street morphology to ambient air quality using six real-world cases. Atmos. Environ. https://doi.org/10.1016/j.atmosenv.2017.05.047.

Shen, Z., Wang, B., Cui, G., Zhang, Z., 2015. Flow pattern and pollutant dispersion over three dimensional building arrays. Atmos. Environ. 116, 202–215. https://doi.org/10.1016/j.atmosenv.2015.06.022.

Shirzadi, M., Naghashzadegan, M.A., Mirzaei, P., 2018. Improving the CFD modelling of cross-ventilation in highly-packed urban areas. Sustain. Cities Soc. https://doi.org/10.1016/j.scs.2017.11.020.

Soulhac, L., Salizzoni, P., 2010. Dispersion in a street canyon for a wind direction parallel to the street axis. J. Wind Eng. Ind. Aerod. 98, 903–910. https://doi.org/10.1016/j.jweia.2010.09.004.

Tominaga, Y., Mochida, A., Murakami, S., Sawaki, S., 2008a. Comparison of various revised k-ε models and LES applied to flow around a high-rise building model with 1:1:2 shape placed within the surface boundary layer. J. Wind Eng. Ind. Aerod. https://doi.org/10.1016/j.jweia.2008.01.004.

Tominaga, Y., Mochida, A., Yoshie, R., Kataoka, H., Nozu, T., Yoshikawa, M., Shirasawa, T., 2008b. AIJ guidelines for practical applications of CFD to pedestrian wind environment around buildings. J. Wind Eng. Ind. Aerod. 96, 1749–1761. https://doi.org/10.1016/j.jweia.2008.02.058.

Tominaga, Y., Stathopoulos, T., 2018. CFD simulations of near-field pollutant dispersion with different plume buoyancies. Build. Environ. 131, 128–139. https://doi.org/10.1016/j.buildenv.2018.01.008.

Tominaga, Y., Stathopoulos, T., 2017. Steady and unsteady RANS simulations of pollutant dispersion around isolated cubical buildings: effect of large-scale fluctuations on the concentration field. J. Wind Eng. Ind. Aerod. 165, 23–33. https://doi.org/10.1016/j.jweia.2017.02.001.

Willemsen, E., Wisse, J.A., 2002. Accuracy of assessment of wind speed in the built environment. J. Wind Eng. Ind. Aerod. https://doi.org/10.1016/S0167-6105(02)00231-3.

World Health Organization, 2016. Summary for Policymakers, World health statistics 2016: monitoring health for the SDGs, sustainable development goals. https://doi.org/10.1017/CBO9781107415324.004.

Xie, Z.T., Castro, I.P., 2009. Large-eddy simulation for flow and dispersion in urban streets. Atmos. Environ. 43, 2174–2185. https://doi.org/10.1016/j.atmosenv.2009.01.016.

Yang, J., Shi, B., Shi, Y., Marvin, S., Zheng, Y., Xia, G., 2020. Air pollution dispersal in high density urban areas: research on the triadic relation of wind, air pollution, and urban form. Sustain. Cities Soc. 101941. https://doi.org/10.1016/J.SCS.2019.101941.

Yang, J., Shi, B., Zheng, Y., Shi, Y., Xia, G., 2019a. Urban form and air pollution disperse: key index and mitigation strategies. Sustain. Cities Soc. https://doi.org/10.1016/j.scs.2019.101955.

Yang, J., Shi, B., Zheng, Y., Shi, Y., Xia, G., 2019b. Urban form and air pollution disperse: key index and mitigation strategies. Sustain. Cities Soc., 101955 https://doi.org/10.1016/j.scs.2019.101955.

You, W., Shen, J., Ding, W., 2017. Improving wind environment of residential neighborhoods by understanding the relationship between building layouts and ventilation efficiency. Energy Procedia 105, 4531–4536. https://doi.org/10.1016/j.egypro.2017.03.972.

Yuan, C., Ng, E., 2014. Practical application of CFD on environmentally sensitive architectural design at high density cities: a case study in Hong Kong. Urban Clim. 8, 57–77. https://doi.org/10.1016/j.uclim.2013.12.001.

Yuan, C., Ng, E., Norford, L.K., 2014a. Improving air quality in high-density cities by understanding the relationship between air pollutant dispersion and urban morphologies. Build. Environ. 71, 245–258. https://doi.org/10.1016/j.buildenv.2013.10.008.

Yuan, C., Ng, E., Norford, L.K., 2014b. Improving air quality in high-density cities by understanding the relationship between air pollutant dispersion and urban morphologies. Build. Environ. https://doi.org/10.1016/j.buildenv.2013.10.008.

Yuan, C., Shan, R., Zhang, Y., Li, X., Yin, T., Hang, J., Norford, L., 2019a. Science of the Total Environment Multilayer urban canopy modelling and mapping for traf fi c pollutant dispersion at high density urban areas. Sci. Total Environ. 647, 255–267. https://doi.org/10.1016/j.scitotenv.2018.07.409.

Yuan, C., Shan, R., Zhang, Y., Li, X.X., Yin, T., Hang, J., Norford, L., 2019b. Multilayer urban canopy modelling and mapping for traffic pollutant dispersion at high density urban areas. Sci. Total Environ. 647, 255–267. https://doi.org/10.1016/j.scitotenv.2018.07.409.

Yuan, C., Shan, R., Zhang, Y., Li, X.X., Yin, T., Hang, J., Norford, L., 2019c. Multilayer urban canopy modelling and mapping for traffic pollutant dispersion at high density urban areas. Sci. Total Environ. 647, 255–267. https://doi.org/10.1016/j.scitotenv.2018.07.409.